AIAA JOURNAL
Vol. 46, No. 11, November 2008

Numerical Investigation of Three-Dimensional Laminar Wall Jet of Newtonian and Non-Newtonian Fluids

K. K. Adane* and M. F. Tachie†
University of Manitoba, Winnipeg, Manitoba R3T 5V6, Canada

DOI: 10.2514/1.37081

Three-dimensional laminar wall jets of a Newtonian fluid and two shear-thinning non-Newtonian fluids were numerically investigated. The complete nonlinear incompressible Navier–Stokes equation was solved using a colocated finite volume based in-house computational fluid dynamics code. For each fluid, the computation was performed at three Reynolds numbers. The results showed that the streamwise velocity profiles for the Newtonian fluid became self-similar but the more shear-thinning fluid never achieved a self-similar condition. Significant differences were observed among the profiles for the various fluids in the inner region. Although the transverse and spanwise components of the velocity decreased substantially with increasing Reynolds number, the values for the non-Newtonian fluids were generally an order of magnitude larger than the corresponding values for the Newtonian fluid. Depending on the specific fluid and Reynolds number, the apparent viscosities were up to 4 orders of magnitude higher than the dynamic viscosity of water. Consequently, the spread of the jet in both the transverse and spanwise directions, decay of the maximum streamwise velocity, and the skin friction coefficient depend strongly on both Reynolds number and nature of the fluid. The results also show that the jet half-width in the transverse direction is significantly higher than in the spanwise direction.

Nomenclature

C_k	=	coefficients
c_f	=	skin friction coefficient
d	=	inlet pipe diameter
m	=	mass fluxes through the control volume faces
n	=	power-law index
p	=	pressure
Re_j	=	Reynolds number based on u_j and d
$Re_{0.5}$, Re_m	=	Reynolds numbers based on u_m, and z_m and $z_{0.5}$
r	=	local radius which is a function of y and z
u, v, w	=	velocity components in streamwise, spanwise, and transverse directions
u_b	=	bulk velocity
u_i	=	velocity component with respect to the Cartesian coordinate x_i
u_j	=	maximum velocity at the exit section of the pipe
u_m, v_m, w_m	=	local maxima values of u v and w
x, y, z	=	streamwise, spanwise, and transverse coordinates
x_i	=	Cartesian coordinates, x, y, z
z_m	=	jet thickness in transverse directions
$z_{0.5}$, $y_{0.5}$	=	jet half-width in transverse and spanwise directions
Δx, Δy, Δy	=	grid points on streamwise, spanwise, and transverse directions
Λ	=	second invariant of the shear-rate tensor
λ	=	consistency index
μ	=	apparent viscosity
μ_w	=	dynamic viscosity of water
ρ	=	density
τ_w	=	friction velocity

Presented as Paper 4163 at the 38th Fluid Dynamics Conference and Exhibit, Seattle, Washington, 23–26 June 2008; received 10 February 2008; revision received 16 June 2008; accepted for publication 16 July 2008.

*Graduate Student, Mechanical and Manufacturing Engineering Department, 75A Chancellors Circle.

†Associate Professor, Mechanical and Manufacturing Engineering Department, 75A Chancellors Circle. Member AIAA.

I. Introduction

A WALL jet can be defined as a shear flow directed along a wall where, by virtue of the initially supplied momentum, at any station, the streamwise velocity over some region within the flow exceeds that in the external stream [1]. There have been numerous studies on two-dimensional (2-D) laminar wall-jet flows, for example, Glauert [2], Bajura and Szewczyk [3], Cohen et al. [4], Gorla and Jeng [5], Filip et al. [6], and Gorla [7]. Three-dimensional (3-D) laminar wall-jet flows (Craft and Launder [8] and Krechetnikov and Lipatov [9]), on the other hand, have received comparably less research attention in spite of their wide and diverse fluid engineering applications. Some of these applications include mass transport enhancement in a bioreactor perfusion system, mixing enhancement in biosensor microfluidic systems, wall-jet detector biosensor, ceramic plasma actuator panels, airless spray painting, control of air contaminants in ecology and process hygiene, and three-dimensional echocardiography (3-D color Doppler) in the quantitative assessment of mitral regurgitation. There is a need, therefore, for additional research to advance understanding of 3-D wall jets. Wall-jet flow is relatively more complex than the free jet or classical near-wall flows such as fully developed channel flows and zero pressure gradient boundary layers. The complexity increases when the flow becomes 3-D and even more complicated when the properties of the fluid medium are not constant, specifically a shear dependence viscosity. It is therefore not surprising that 3-D wall-jet flows of non-Newtonian fluid have not received research attention.

Tetervin [10] and Glauert [2] carried out analytical studies on two-dimensional laminar wall-jet flow. They showed that the local maximum velocity (u_m) decays as one-half power while the jet half-width increases as three-quarter power of the downstream distance. Subsequently, a number of experimental and numerical investigations have been conducted to understand the characteristics of both laminar and turbulent wall jets. Most of these studies involved heat transfer, stability analysis, effects of compressibility, blowing and suction as well as moving and ribbed walls on the flow dynamics (Bajura and Szewczyk [3], Cohen et al. [4], Gorla [11], Issa [12,13]). Bajura and Szewczyk [3], for example, employed a hot-wire anemometer to study 2-D laminar wall-jet flow at various Reynolds numbers (250–800). Their results showed that the flow becomes self-similar at 18 slot heights downstream of the nozzle outlet for a jet-exit Reynolds number (based on the slot height) of 377. They reported similarity exponents that were in good agreement with theoretical values reported by Glauert [2]. Cohen et al. [4]

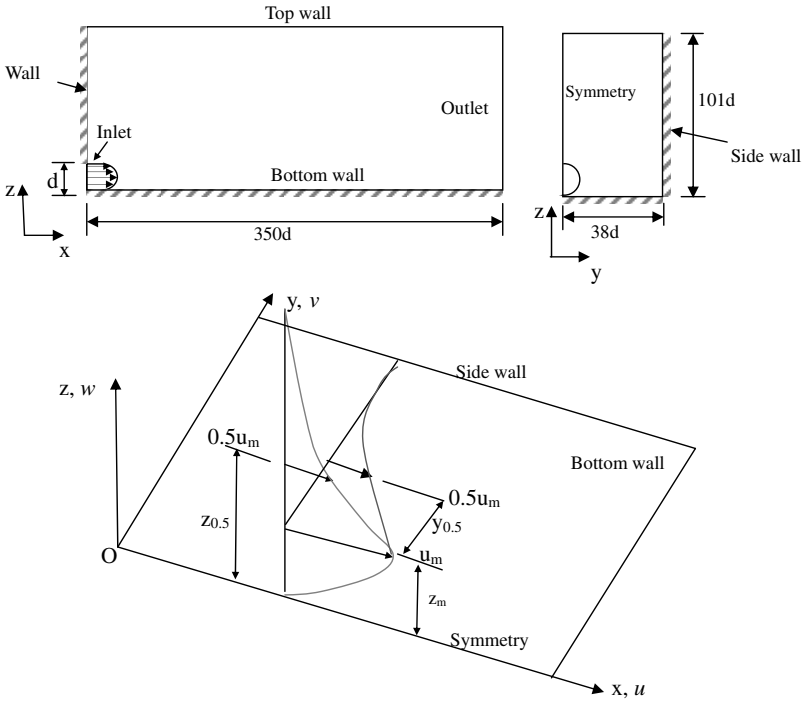

Fig. 1 Schematic of the present flow geometry.

investigated laminar-turbulent transition of 2-D wall jets subjected to blowing and suction using experimental and analytical techniques. The experiments were performed at Reynolds numbers of 466–725. They found that the velocity profiles become self-similar after 30 slot heights downstream of the nozzle. Gorla and Jeng [5] numerically analyzed a 2-D laminar plane wall jet and obtained an explicit expression for several parameters including potential core length, jet half-width, maximum velocity, similarity exponents, exterior momentum flux, and skin friction coefficients as functions of jet Reynolds numbers. Issa [12,13] applied a commercial computational fluid dynamics (CFD) code, Fluent, to numerically study a 2-D laminar wall jet. He applied various velocity and temperature profiles at the inlet. A very good agreement with Glauert's theoretical results was observed. In addition, the local and overall skin friction coefficients were found to depend on the Reynolds number.

Craft and Launder [8] obtained numerical solutions for a self-similar condition as well as the parabolic form of the governing equations for 3-D laminar wall-jet flow. It was reported that there was no substantial streamwise vorticity so that the ratio of the spanwise to transverse spread rates was substantially less than unity. Based on this observation, they concluded that, for the case of the laminar wall jet, viscous diffusion is principally responsible for the growth of the jet in the flow direction. The spreads of the jet in the transverse and spanwise directions were found to depend on the Reynolds number.

Most of the prior investigations on wall-jet flow of non-Newtonian fluids have focused on the 2-D case. Filip et al. [6] performed a similarity analysis for 2-D laminar wall jets of power-law fluids past axisymmetric bodies. The similarity profile was observed to be fluid dependent; that is, in the inner and outer regions, the shear-thinning fluid has higher velocities and the shear thickening fluid has lower velocities than a Newtonian fluid. Gorla [7] performed an analytical study on a 2-D laminar wall jet of power-law non-Newtonian fluid over curved surfaces. It was observed that the velocity profile and skin friction coefficient depend on the shape of the surface. Furthermore, the local skin friction coefficient values decrease as the fluid becomes more shear thinning or shear thickening.

Although the 2-D laminar wall jet has been studied extensively (especially for Newtonian fluids), only a few investigations of the 3-D laminar wall jet have been reported. For a 2-D laminar wall jet of Newtonian fluid, it has been shown that the velocity profile becomes self-similar beyond a downstream location that depends strongly on jet Reynolds number [3,4]. For the 2-D laminar wall jet of non-Newtonian fluids, prior analytical solutions have shown the existence of a similarity condition. Furthermore, the skin friction depends highly on the nature of the non-Newtonian fluid [7]. The purpose of this paper is to numerically study the effects of the Reynolds number on the velocity profiles, the decay of the local maximum velocities, and the spread of the 3-D laminar wall jet of both Newtonian and non-Newtonian fluids. The numerical approach is to solve accurately the full nonlinear Navier–Stokes equations. A schematic of the flow geometry (half-section), nomenclature, and coordinate system are shown in Fig. 1. The inlet pipe is of diameter $d = 2.68$ mm, while the main channel has a length of $350d$, height of $101d$, and width of $76d$. In the coordinate system used here, streamwise, spanwise, and transverse directions are referred to the x, y, and z axes, respectively. As shown in Fig. 1, $x = 0$ at the inlet, $y = 0$ at the plane of symmetry, and $z = 0$ on the bottom wall.

II. Computational Method

A. Governing Equations

The governing equations for steady, incompressible flow in tensor form are given in Eqs. (1) and (2).

Table 1 Inlet velocities

Re_j	$n = 1.00$		$n = 0.702$		$n = 0.44$	
	u_j, mm/s	u_b, mm/s	u_j, mm/s	u_b, mm/s	u_j, mm/s	u_b, mm/s
77	0.029	0.014	3.323	1.821	14.965	9.288
155	0.058	0.029	5.696	3.121	23.433	14.545
310	0.116	0.058	9.717	5.324	36.543	22.682

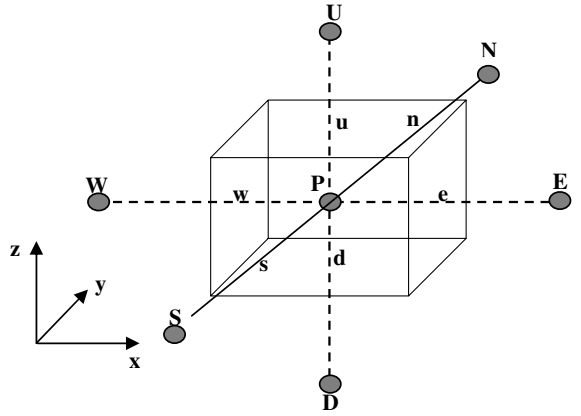

Fig. 2 Typical control volume and labeling scheme.

Continuity equation:

$$\frac{\partial u_i}{\partial x_i} = 0 \tag{1}$$

Momentum equation:

$$\rho u_j \frac{\partial u_i}{\partial x_j} = \frac{\partial}{\partial x_j}\left[\mu\left(\frac{\partial u_i}{\partial x_j} + \frac{\partial u_j}{\partial x_i}\right)\right] - \frac{\partial p}{\partial x_i} \tag{2}$$

where u_i represents the velocity component with respect to the Cartesian coordinate x_i, p is the pressure, μ is dynamic viscosity, and ρ is the density that is assumed to be constant. For non-Newtonian fluids, the viscosity is not constant, and it is here assumed to be a function of the shear-rate only. A generalized shear-thinning power law ($\mu = \lambda\Lambda^{(n-1)}$) given by Bird et al. [14] is used in the present study. Here, λ is the consistency index, n is the power-law index, and Λ is the second invariant of the shear-rate tensor, given as

$$\Lambda = [2\{(\partial u/\partial x)^2 + (\partial v/\partial y)^2 + (\partial w/\partial z)^2\} + (\partial u/\partial y + \partial v/\partial x)^2 + (\partial u/\partial z + \partial w/\partial x)^2 + (\partial v/\partial z + \partial w/\partial y)^2]^{1/2} \tag{3}$$

The wall-jet flow is characterized by the Reynolds number, $Re_j (= \rho u_j^{2-n} d/\lambda)$ at the pipe exit, where u_j is the maximum velocity at the exit section of the pipe. It should be noted that a Newtonian fluid can be considered as a special case of the non-Newtonian fluid. In this case, $n = 1$, while the consistency index λ becomes the dynamic viscosity of the fluid.

B. Boundary Conditions

The boundary conditions used for the computation domain shown in Fig. 1 are as follows:

1) Inlet ($x = 0$): $u(r)/u_b = (3n + 1)[1 - (2r/d)^{(n+1)/n}]/(n + 1)$ in the region $0 < z < d$ and $0 < y < 0.5d$; otherwise, $u = v = w = 0$. Note that $u_b (= u_j[n + 1]/[3n + 1])$ is the bulk velocity, n the is power-law index, and r is the local radius which is a function of y and z.

2) Outlet ($x = 350d$): $p_{\text{spec}} = 0$.

3) Symmetry plane ($y = 0$): $\mathrm{d}u/\mathrm{d}y = \mathrm{d}v/\mathrm{d}y = \mathrm{d}w/\mathrm{d}y = 0$.

4) Side wall ($y = 38d$): $u = v = w = 0$.

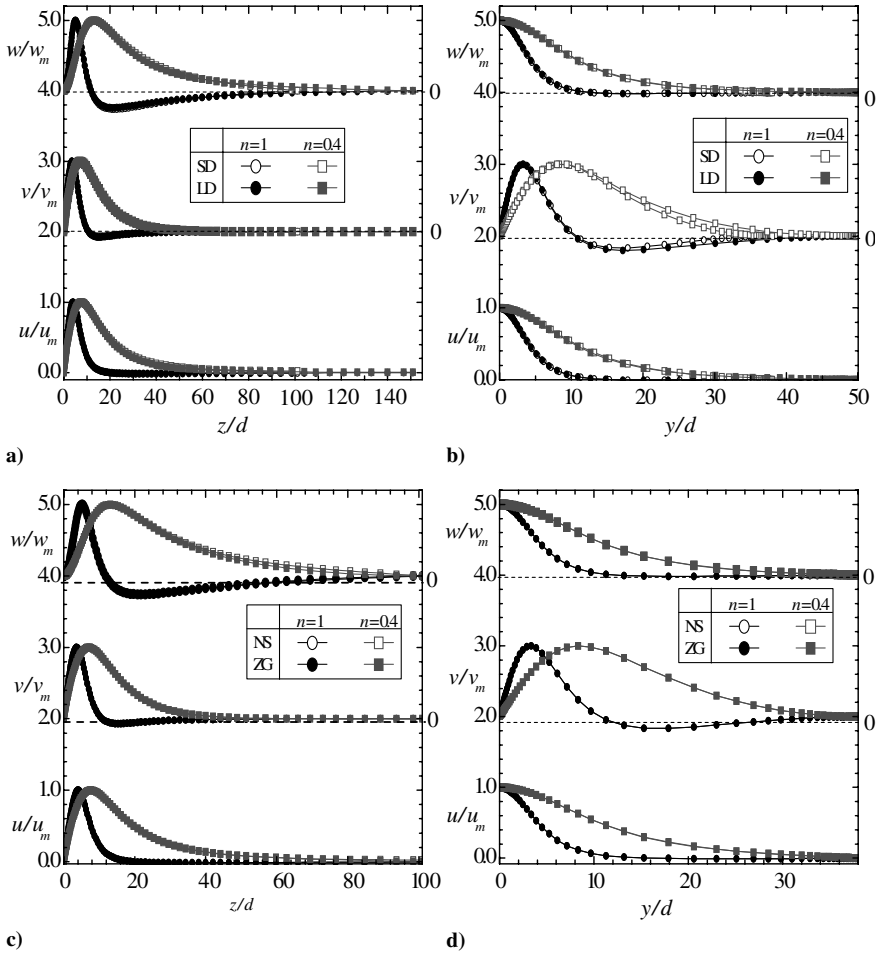

Fig. 3 a) and b) show comparison between velocity profiles obtained using a smaller flow domain, SD ($350d \times 38d \times 101d$) and a larger flow domain, LD, size ($350d \times 50d \times 151d$). c) and d) show a comparison between profiles obtained using the no-slip boundary condition, NS ($u = v = 0$) and zero gradient, ZG ($\mathrm{d}u/\mathrm{d}z = \mathrm{d}v/\mathrm{d}z = 0$), at the top wall ($z = 101d$). Note that all profiles were obtained for $Re_j = 77$ and at $x/d = 20$.

Table 2 Mesh sizes in mm

Mesh	Δx (min, max)	Δy (min, max)	Δz (min, max)
Coarse	1.60×10^{-4}, 6.22×10^{-3}	8.38×10^{-5}, 7.0×10^{-3}	8.93×10^{-5}, 9.00×10^{-3}
Medium	5.72×10^{-5}, 6.00×10^{-3}	7.44×10^{-5}, 4.83×10^{-3}	7.88×10^{-5}, 7.36×10^{-3}
Fine	6.13×10^{-6}, 7.6×10^{-3}	5.44×10^{-5}, 3.04×10^{-3}	5.88×10^{-5}, 5.27×10^{-3}

5) Bottom wall ($z = 0$): $u = 0$, $v = 0$, and $w = 0$.

6) Top wall ($z = 101d$): $du/dz = dv/dz = 0$, and $w = 0$.

It should be noted that a first-order approximation was employed to obtain u and v at $z = 101d$. The normal velocity to the outlet ($x = 350d$), u was obtained by a mass balance for each cell. The viscosity at the boundaries was obtained by linear extrapolation from the two nearest neighboring cells. The same method was used for pressure at all boundaries except at the outlet where the pressure value was prescribed, Ferziger and Perić [15]. The rheological data for the power-law non-Newtonian fluids from Wu and Thompson [16] and Dressler [17] were used for the two non-Newtonian fluids studied in this paper. These are $n = 0.44$, $\rho = 1000$ kg/m^3, $\lambda = 2.37$ Pa $\cdot$ s^n, $n = 0.702$, $\rho = 1090$ kg/m^3, and $\lambda = 0.1803$ Pa $\cdot$ s^n. Table 1 provides a summary of the exit jet velocity (u_j) and the corresponding bulk velocity (u_b) for all the fluids and Reynolds numbers investigated.

In addition to the flow domain described earlier (i.e., length of $350d$, height of $101d$, and width of $38d$), computation was also performed for two test fluids ($n = 0.4$ and $n = 1$) with a larger flow domain size (length of $350d$, height of $151d$, and width of $50d$). The rationale was to determine if the domain size used in the present study is large enough. The lowest Reynolds number was employed in the exploratory study because it was expected that the spread of the jet would be fastest at this Reynolds number. As will be shown subsequently (see Figs. 3a and 3b), no significant differences were observed among the results from both flow domain sizes. Computation was also carried out by using the no-slip boundary condition ($u = v = 0$) at the top wall instead of the zero velocity gradient ($du/dz = dv/dz = 0$) at $z/d = 101$. The results from both boundary conditions were identical (see Figs. 3c and 3d). Because the zero gradient boundary condition produced better convergence and stability of the solver, it was employed in all the results presented

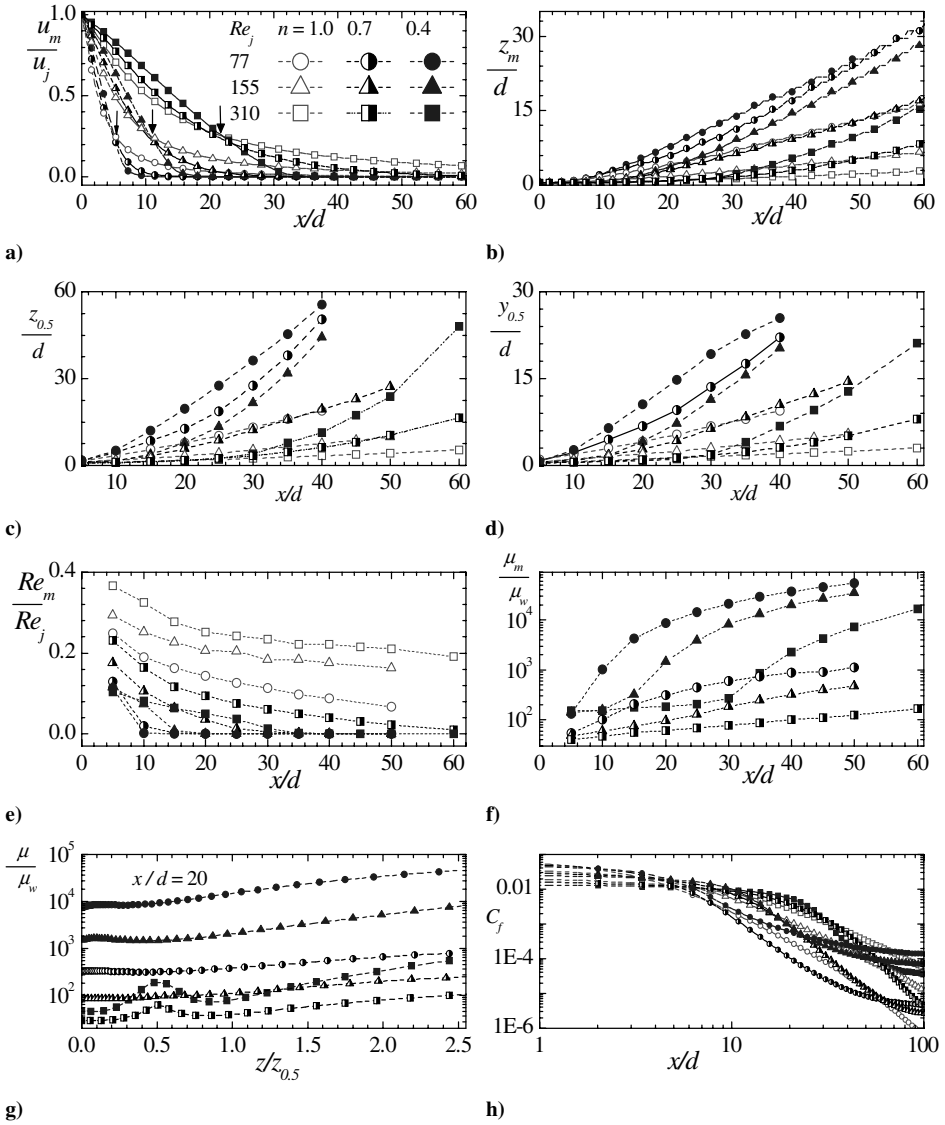

Fig. 4 a) Maximum velocity decay u_m; b) z_m variation in downstream direction; c) and d) are jet half-widths, variation of e) Re_m/Re_j; f) μ_m/μ_w; g) μ/μ_w; and h) C_f.

subsequently in this paper. The results presented will be confined to the first $100d$ of the $350d$ to avoid the possibility of any influence of the outer boundary conditions.

C. Discretization Method

The conservation Eqs. (1) and (2) were discretized using a colocated finite-volume method for general orthogonal grids which is described in detail in Ferziger and Perić [15]. Here, only a brief summary is provided. The usual integration of the differential equations is performed over control volumes with the dependent variable held at P as shown in Fig. 2. The neighboring nodal values are held at W, E, S, N, D, and U (west, east, south, north, down, and up), whereas the face values are held at w, e, s, n, d, and u. The standard central difference scheme (CDS) is used for the diffusion terms. To achieve a more accurate representation of the convective terms, the CDS has been implemented in the form of a deferred correction [18] to the first-order upwind approximation (UDS). The main advantages of the deferred correction are stability, simplicity, and computer-memory saving. The deferred correction approach tends to promote numerical stability as it ensures that the coefficient matrix is (more) diagonal dominant. The discretization of Eqs. (1) and (2), therefore, takes the form:

$$\dot{m}_e + \dot{m}_n + \dot{m}_u - \dot{m}_w - \dot{m}_s - \dot{m}_d = 0 \tag{4}$$

$$C_P u_{i,P} + \sum_k C_k u_{i,k} = b_\phi \tag{5}$$

where the index k runs over the six nearest neighbors (W, E, S, N, D, and U) of node P, $\dot{m}$ and u_i (u, v, and w) are the mass fluxes through the control volume faces and nodal velocity, respectively; the coefficient C_k consists of a contribution from the implicitly treated parts of both convection and diffusion fluxes, whereas b_ϕ contains the pressure term for respective velocity component and the explicitly treated parts of convection and diffusion. It should be mentioned that at convergence the UDS terms are expected to cancel out leaving only CDS terms. The underrelaxation parameter was incorporated to account for the nonlinear nature of the equation systems and stability of the solver [19].

Pressure-velocity coupling on the colocated grid was achieved with an interpolation scheme suggested by Rhie and Chow [20]. A segregated solution approach using the semi-implicit method for pressure-linked equation consistent (SIMPLEC) algorithm [21] was used. A Poisson equation solved for the pressure-correction field by enforcing mass conservation is as follows:

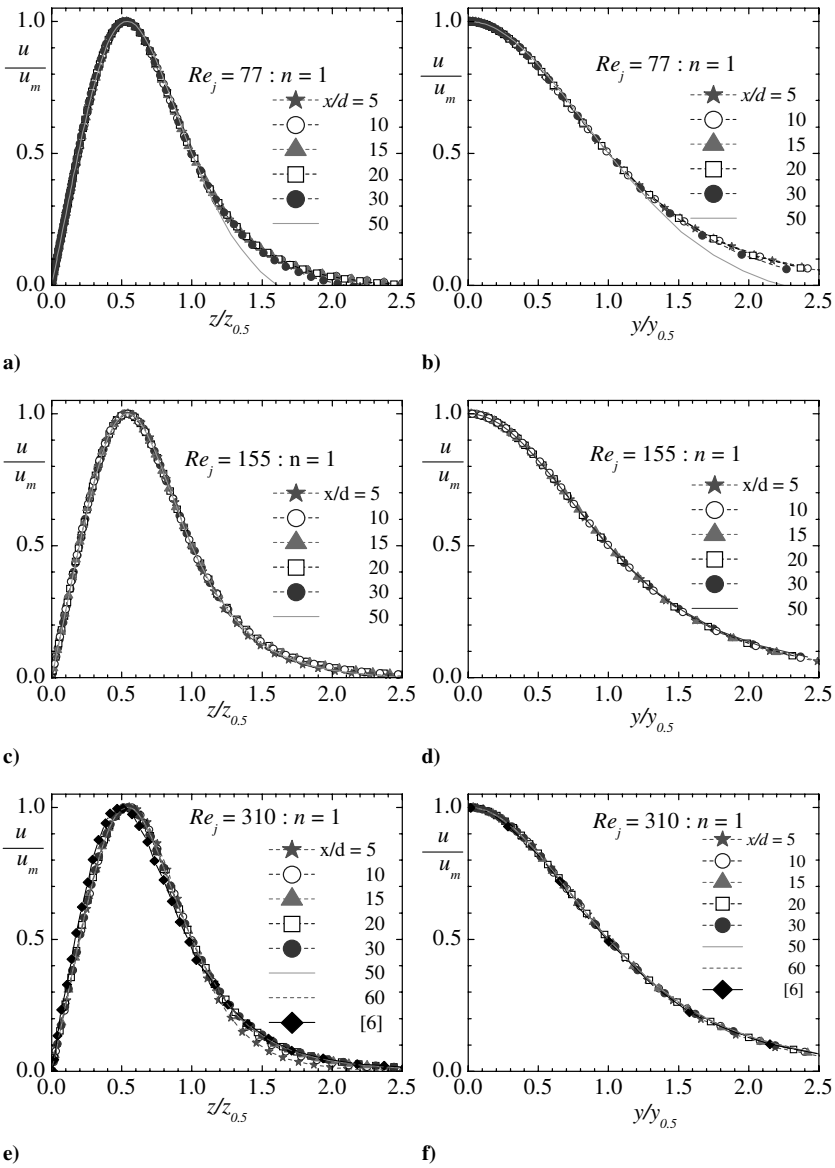

Fig. 5 Normalized streamwise velocity profiles on transverse a), c), and e) and spanwise directions b), d), f) at various downstream locations for the Newtonian fluid.

$$C_P p_P + \sum_k C_k p_k = b_m \tag{6}$$

where b_m is an artificial mass source for each control volume left after mass conservation, and $C_{kb(=P,W,E,S,N,D,U)}$ are the pressure-correction coefficients. The boundary velocities are assumed to be prescribed and are not corrected except those boundaries where pressure values are prescribed. This condition is equivalent to specifying a zero gradient on the pressure correction. The velocities on pressure prescribed boundaries are, however, corrected.

D. Solution Procedure

The resulting algebraic equations (5) and (6) for nodal velocities and pressure correction, respectively, were solved using a 3-D version of the strongly implicit procedure (SIP) solver [22]. The solution algorithm consists of a sequential solution of the three discretized momentum equations and the pressure-correction equation. The velocities, mass fluxes, and pressure are then corrected. These values are used to update the coefficients and calculate the viscosity in the case of non-Newtonian fluid for the next outer iteration. The viscosity is thus treated explicitly. For each SIMPLEC iteration (outer iteration), up to five and 15 SIP iterations are performed for each velocity component and pressure field, respectively. The SIP iterations are stopped if the residual level drops by a factor of 5 for velocity components and 10 for the pressure-correction equation. A solution to a tighter tolerance yielded no advantage because the variables need to be updated in outer iterations. The convergence criterion which is the residual norm (the sum of absolute residuals over all control volumes) for each equation was set to 10^{-4}.

The code that implements the numerical model was checked thoroughly for internal consistency. Test cases of a lid-driven cavity described by Lilek et al. [23] and 3-D laminar wall-jet flow by Craft and Launder [8] were used to validate the code. In addition, computations for a fully developed channel flow for both Newtonian fluid and non-Newtonian fluid having identical properties as used in the present study and in Dressler [17] were performed. In all the test cases, very good agreement was obtained. A comparison between the results from the 3-D laminar wall-jet results by Craft and Launder [8] and those obtained in the present study will be presented in Sec. III.B.

A number of grid meshes were used to determine grid independence of the solutions. The grid independence tests were conducted using grids made up of coarse ($150 \times 38 \times 63$), medium ($250 \times 58 \times 95$), and fine ($400 \times 111 \times 181$) grids in the streamwise, spanwise, and transverse directions, respectively. The grids

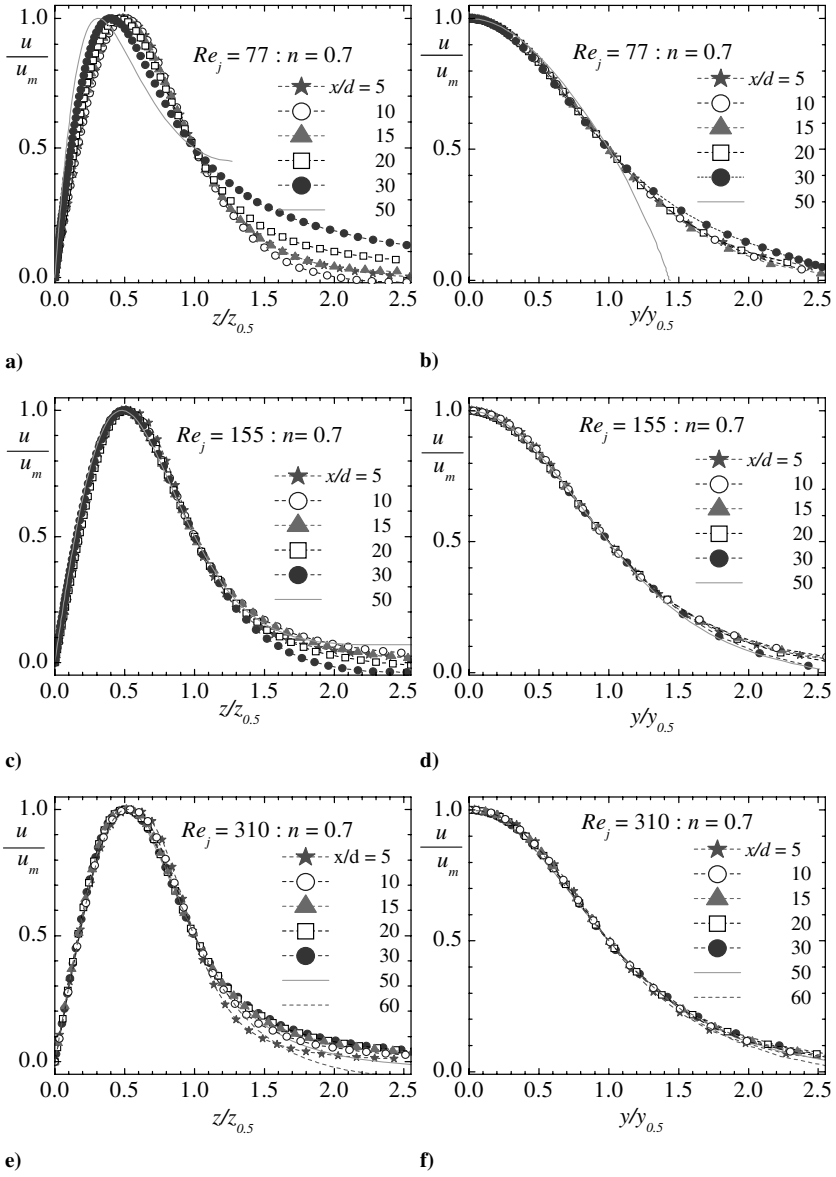

Fig. 6 Normalized streamwise velocity profiles on transverse a), c), and e) and spanwise directions b), d), and f) at various downstream locations for the $n = 0.7$ non-Newtonian fluid.

were geometrically expanded in all three directions. The absolute values of the maximum and minimum grid sizes (Δx, Δy, and Δz) are given in Table 2.

Based on the jet half-widths in the transverse and spanwise directions, the maximum difference between the coarse and medium grids at selected locations was 4.3%. In terms of typical local velocity profiles examined at $x/d = 20$, the maximum percentage changes were 7.3% that occur in the u_m values. The corresponding differences between the medium and fine grids were 0.88 and 1.2%, respectively. Based on these tests, the medium grid was used for the present work. All the simulations were performed on a Sun V20z machine with 4031 MB memory.

E. Effects of Flow Domain Sizes and Boundary Conditions

As mention in Sec. II.B, the effects of computation flow domain sizes on the results were explored. Typical profiles of u, v, and w in the transverse and spanwise directions for the Newtonian fluid ($n = 1$) and a non-Newtonian fluid ($n = 0.4$) are shown in Figs. 3a and 3b, respectively. The profiles shown in the figure were obtained for the lowest Reynolds number ($Re_j = 77$) and at $x/d = 20$. Except for small differences in the outer region of the v profiles (Fig. 3b), the results from both domain sizes are nearly indistinguishable. Figures 3c and 3d compare results obtained when the boundary condition at the top wall ($z = 101d$) is changed from zero velocity gradient to a no-slip boundary condition. For all three velocities and in both the transverse and spanwise directions, the results from two boundary conditions are in excellent agreement.

III. Results and Discussion

A. Decay of Maximum Streamwise Velocity, Spread Rates, and Skin Friction Coefficient

Before the discussion on the velocity profiles in the transverse and spanwise directions for the three different fluids and the three Reynolds numbers, a number of parameters are used to characterize the flow development in the streamwise direction. These include the local maximum streamwise velocity (u_m), the location of u_m from the wall (z_m), the jet half-width in the transverse direction ($z_{0.5}$), and the spanwise direction ($y_{0.5}$). The jet half-widths ($z_{0.5}$ and $y_{0.5}$) are defined as the distance measured from the origin to the respective location at which u is one-half of u_m. It should be recalled that the origins for z and y are located on the bottom wall and symmetry plane, respectively (Fig. 1). The variation of u_m for the various fluids and Reynolds number with streamwise distance from the jet exit will provide insight into how the decay of the velocity field depends on fluid type and Reynolds number. Similarly, $y_{0.5}$ and $z_{0.5}$ are used,

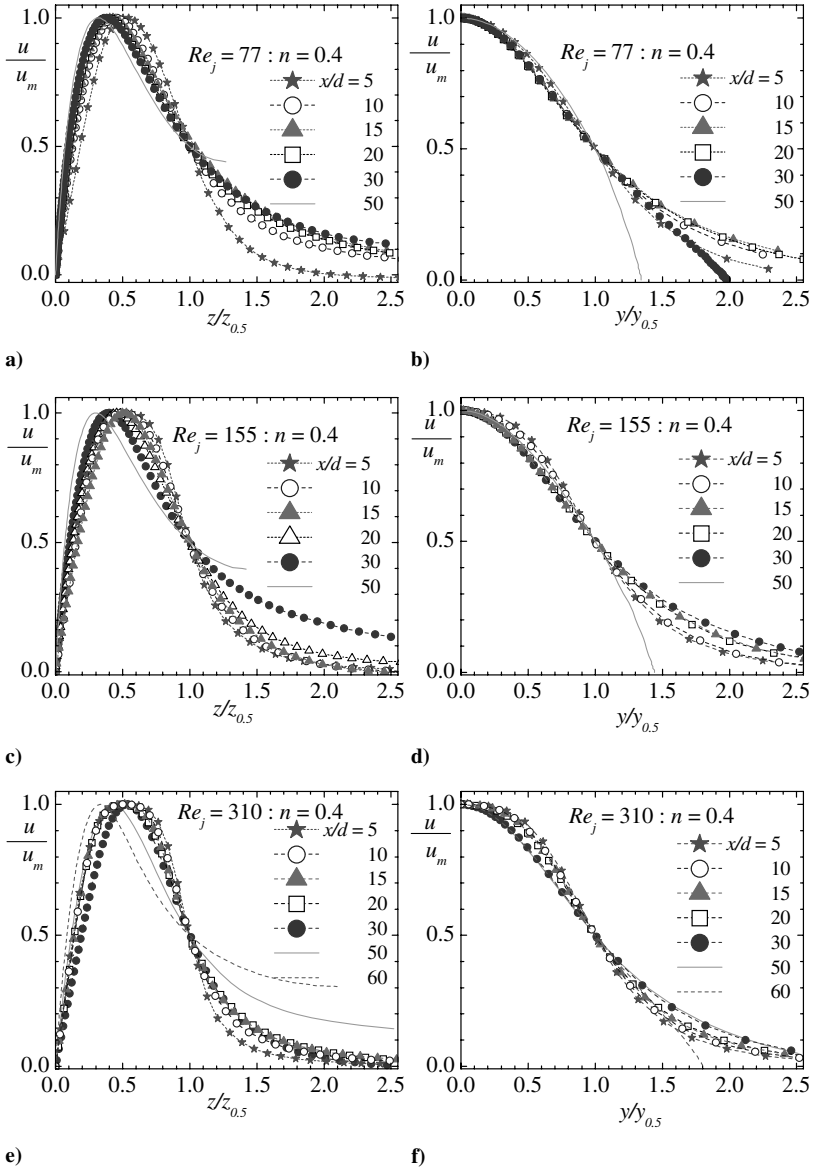

Fig. 7 Normalized streamwise velocity profiles on transverse a), c), and e) and spanwise directions b), d), and f) at various downstream locations for the $n = 0.4$ non-Newtonian fluid.

respectively, to document the effects of fluid type and Reynolds number of the growth or spread of the jet in the spanwise and transverse directions, whereas z_m represents the thickness of the inner layer that is akin to a classical boundary layer. In the following presentation, u_j will be used as the appropriate velocity scale and the inlet pipe diameter d is used to normalize distances in the streamwise, spanwise, and transverse directions. The Newtonian fluid will be denoted by $n = 1.0$, while the two non-Newtonian fluids will be denoted by $n = 0.7$ and $n = 0.4$.

The variations of u_m/u_j with x/d are shown in Fig. 4a. As the jet evolves downstream, it entrains the stagnant ambient fluid and the jet velocity is slowed considerably. This is true for all the fluids and the Reynolds numbers. The decay of u_m is most rapid for the lowest Reynolds number and slowest for the highest Reynolds number investigated. At each Reynolds number, the profiles plotted in Fig. 4a can be divided into two regions: 1) an initial region where the decay is most rapid for $n = 1.0$ and slowest for $n = 0.4$ and 2) a final region where the decay is most rapid for $n = 0.4$ and slowest for $n = 1.0$. The demarcation between these regions, which is indicated by arrows in the figure, occurred at $x/d = 5$, 10, and 22, respectively, for $Re_j = 77$, 155, and 310. Figure 4a also demonstrates that, at $x/d = 10$, the values of u_m/u_j for $n = 1.0$ and $n = 0.4$ at $Re_j = 77$ are only 11 and 0.7%, respectively. The corresponding values of u_m/u_j at $x/d = 30$ and $Re_j = 310$ are 18 and 4%, respectively. When u_m becomes negligibly small, the velocity distribution becomes more uniform and the flow may begin to lose its wall-jet characteristics. These results imply that, for a particular fluid such as $n = 1$, the jet with the least momentum (lowest Re_j) would vanish at a smaller x/d location whereas at similar Re_j, the fluid with the smallest n would vanish at a smaller x/d.

Figures 4b–4d show that the decay of u_m is accompanied by a growth or an increase in z_m, $z_{0.5}$, and $y_{0.5}$ with downstream distance. The growth rate is also Reynolds number and fluid dependent. More specifically, for a similar fluid, the jet spreads faster at a lower Re_j, and for a similar Re_j, the non-Newtonian fluids ($n = 0.4$ and 0.7) spread faster than the Newtonian fluid ($n = 1.0$). In spite of an increase in both $y_{0.5}$ and $z_{0.5}$ with x/d and the strong dependence on the jet Reynolds number and fluid type, it was observed that $y_{0.5}/z_{0.5} = 0.5 \pm 0.15$. The implication is that the jet spreads more rapidly in the transverse direction than it does in the spanwise direction. As reported by Craft and Launder [8], the significant differences between $z_{0.5}$ and $y_{0.5}$ are due to the fact that there is no substantial streamwise vorticity. The faster spread rates at the lower Reynolds numbers and for the non-Newtonian ($n = 0.7$ and 0.4) fluids are possibly due to viscous diffusion effect and significantly higher secondary flows.

To explain the above observation, the local Reynolds numbers, $Re_m = \rho u_m z_m/\mu_m$, for all the fluids and Reynolds numbers are

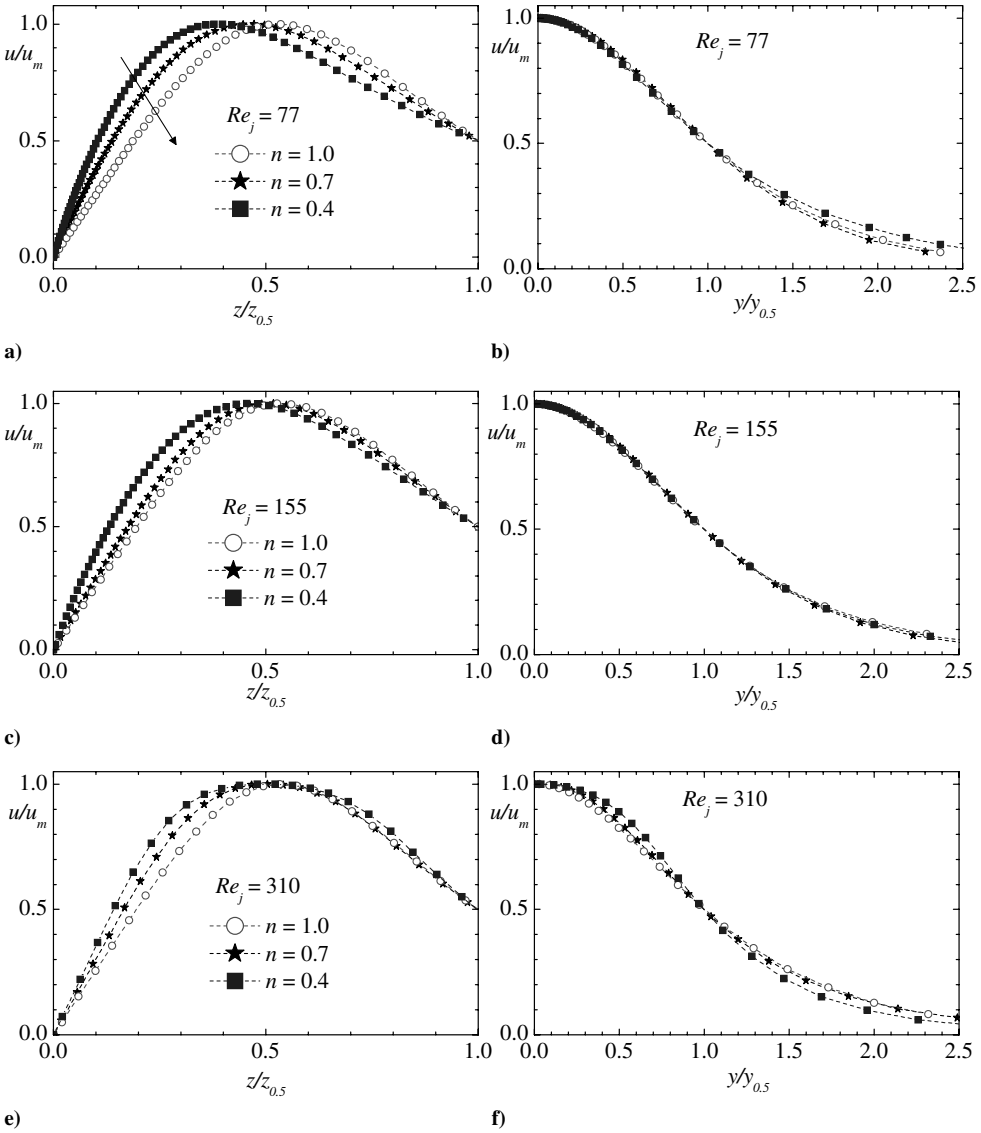

Fig. 8 Comparison of velocity profiles on transverse a), c), and e) and spanwise directions b), d), and f) at various downstream locations for Newtonian and non-Newtonian fluids.

plotted in Fig. 4e. Unlike the Newtonian fluid for which μ does not vary within the flowfield, the apparent viscosity for the non-Newtonian fluids depends on the shear rate. In the above expression, μ_m is the specific value of the apparent viscosity evaluated at z_m from the expression $\mu = \lambda\Lambda^{(n-1)}$, where Λ is calculated using Eq. (3), and values of λ stated earlier for the fluids are used. It is clear that the values of Re_m (and $Re_{0.5}$ which are not shown) decrease downstream as the flow develops. The fastest decrease occurs at $Re_j = 77$ and the lowest decrease occurred at $Re_j = 310$. Furthermore, for the same Re_j, both Re_m and $Re_{0.5}$ decreased more rapidly for the non-Newtonian fluids ($n = 0.7$ and 0.4) than the Newtonian fluid ($n = 1$). Since μ is constant for the Newtonian fluid, Fig. 4e supports the notion that u_m decays faster with x than z_m increases with x. Perhaps a more important observation from Fig. 4e is that, notwithstanding the substantially higher values of z_m for the $n = 0.7$ and 0.4 fluids compared with the Newtonian fluid ($n = 1$), values of Re_m are dramatically lower for the $n = 0.7$ and 0.4 fluids than for $n = 1$. The reduced values of Re_m for the non-Newtonian fluids are due to the substantially higher values of μ_m. These values, normalized by the dynamic viscosity of water ($\mu_w = 1.0 \times 10^{-3}$ N · s/m^2), which is the Newtonian fluid used in the present study, are plotted in Fig. 4f. First of all, the apparent viscosity is up to 4 orders of magnitude higher than μ_w. The values are substantially higher for the more shear-thinning fluid ($n = 0.4$), and for a given fluid, μ_m/μ_w increases with decreasing Re_j. Figure 4g shows plots of representative distributions of μ/μ_w with transverse distance ($z/z_{0.5}$) at midspan and $x/d = 20$ for $Re_j = 77$, 155, and 310. The effects of fluid type and Reynolds number on these profiles are qualitatively similar to the observation made in Fig. 4f.

The wall shear stress distribution at the symmetry plane ($y = 0$) is presented using the skin friction coefficient, $C_f (= \tau_w / 0.5\rho u_j^2)$, where $\tau_w = \mu|\mathrm{d}u/\mathrm{d}z|$. The data presented by Gorla [7] suggest that C_f values decrease as the fluid becomes more shear thinning or thickening. The skin friction coefficient also depends on the jet Reynolds number and viscosity of the fluid [2]. The present data (Fig. 4h) show that, in the early region of flow development ($x/d < 5$), Reynolds number effects are more dominant than the fluid type. In this region, C_f increases with increasing Re_j. For $Re_j = 155$ and 310, the skin friction is slightly higher for the Newtonian fluid compared with the non-Newtonian fluids. The results in this region are, therefore, consistent with the findings of Gorla [7]. However, C_f values at the lower Re_j decrease most rapidly and in the region $6 \le x/d \le 23$ for the non-Newtonian fluid with $n = 0.4$, the C_f values are consistently higher for a higher Re_j. Similarly, for $n = 0.7$, the C_f values are consistently higher for a higher Re_j in the region $6 \le x/d \le 60$ and at all x/d locations examined for the Newtonian fluid ($n = 1.0$). In these latter regions, C_f does not show any systematic dependence on the type of fluid. It should be noted

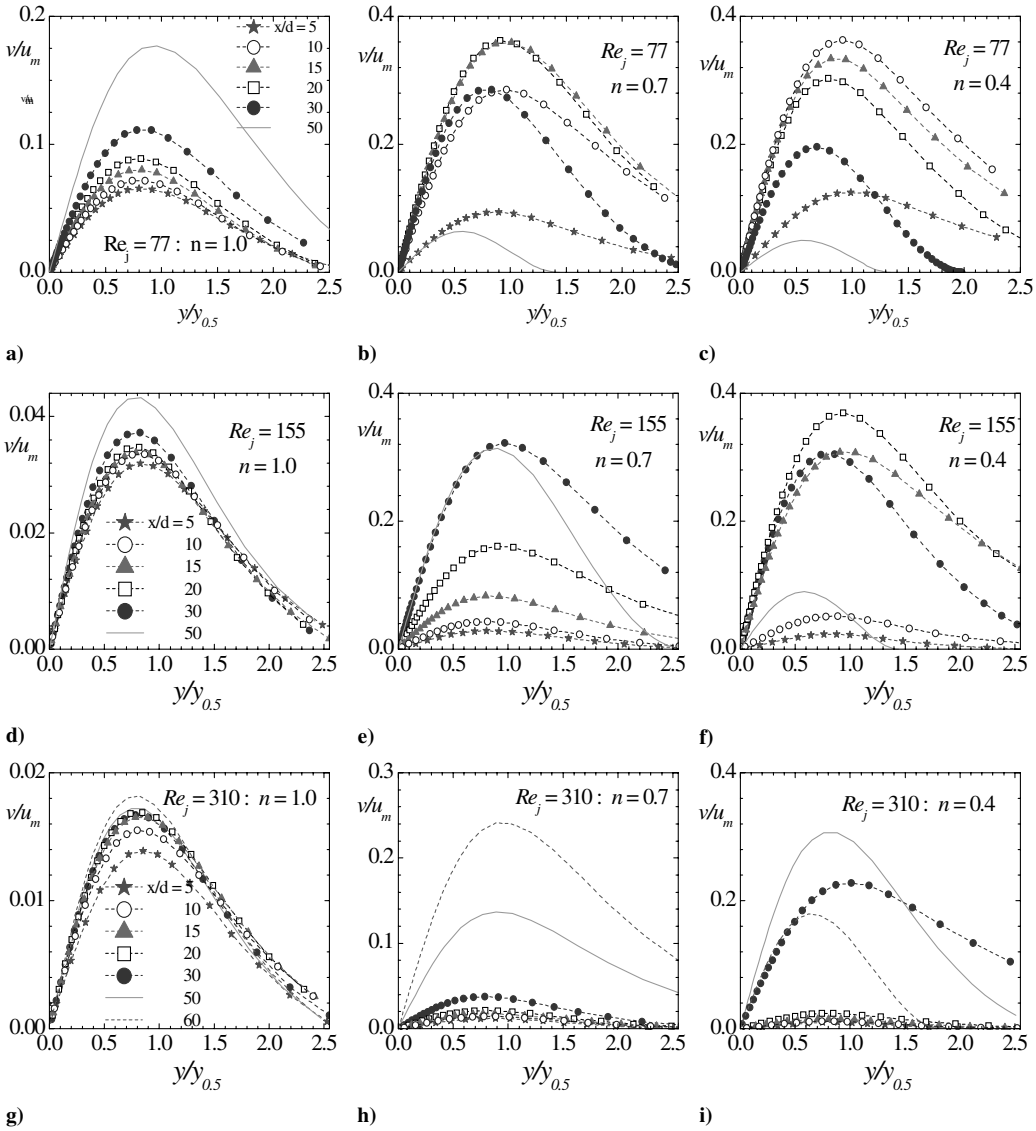

Fig. 9 The v-velocity profiles in spanwise direction at various downstream locations for Newtonian a), d), and g) and non-Newtonian fluids $n = 0.7$ b), e), and h) and $n = 0.4$ c), f), and i).

that at the downstream limit of the above regions, the C_f values are almost negligible. It is believed that the decreasing x/d limit with decreasing n is possibly due to the notion that the jet decayed fastest for the smallest n (as the fluid becomes more shear thinning) and may therefore disappear at the smallest x/d.

B. Velocity Distribution and Similarity Consideration

The streamwise velocity profiles on the symmetry plane ($y = 0$) and along z_m at various normalized streamwise locations ($x/d = 5$–60) are shown in Fig. 5 for the Newtonian fluid ($n = 1$). The jet half-widths $z_{0.5}$ and $y_{0.5}$ are used, respectively, to normalize the transverse distance measured from the bottom wall and the spanwise distance measured from the symmetry plane. At each downstream location, the velocity increases transversely from zero at the wall to a maximum u_m at distance z_m from the wall and then decreases progressively to zero (Figs. 5a, 5c, and 5e). A similar trend was observed in the spanwise direction where u/u_m decreases from 1 to nearly zero, Figs. 5b, 5d, and 5f. This trend is the same for all three Reynolds numbers. For the Reynolds numbers and axial locations shown in the figure, the velocity profiles in the transverse direction collapsed onto a single curve (the only exceptions are the profiles at $x/d = 50$ for $Re_j = 77$ and at $x/d = 5$ for $Re_j = 310$, both in the outer region $z/z_{0.5} > 1$). The collapse of the profiles in the spanwise direction is similarly remarkable, irrespective of the Reynolds number. Figures 5e and 5f show that the previous numerical results from Craft and Launder [8] at identical Reynolds number ($Re_j = 310$) are in very good agreement with the present results. Irrespective of the Reynolds number, the maximum velocity occurred at $z_m/z_{0.5} \approx 0.5$. These results imply that, for the Newtonian fluid, similarity in both the transverse and spanwise directions is achieved as early as $x/d = 5$. For 2-D wall-jet flow of the Newtonian fluid, the onset of self-similarity was found to be $x/d = 18$ (Bajura and Szewczyk [3]) for $Re_j = 377$ and $x/d = 18$ (Cohen et al. [4]) for $Re_j = 466$–725.

Similar observations are found for the spanwise profiles of non-Newtonian fluid with $n = 0.7$ (Figs. 6b, 6d, and 6f). For $Re_j = 155$ and 310, the transverse profiles in the region $z/z_{0.5} < 1$ are also in excellent agreement, and $z_m/z_{0.5} \approx 0.5$. At the lowest Reynolds number ($Re_j = 77$), however, the transverse profiles do not show any consistent behavior. Significant discrepancies are observed both in the inner and outer regions. For example, as x/d increases, $z_m/z_{0.5}$ moves closer to the wall. It is tempting to conclude that there is a genuine lack of self-similarity for the $n = 0.7$ fluid at $Re_j = 77$. For the $n = 0.4$ fluid (Fig. 7), agreement among profiles at various x/d is lacking and the location of the maximum velocity ($z_m/z_{0.5}$) is not fixed. Although profiles at two or three x/d locations for a given Reynolds number may collapse reasonably well, given the overall trends observed in the figures it is not possible to conclude that the profiles are self-similar. It is not clear if the lack of satisfactory agreement (or possible lack of similarity) for the non-Newtonian

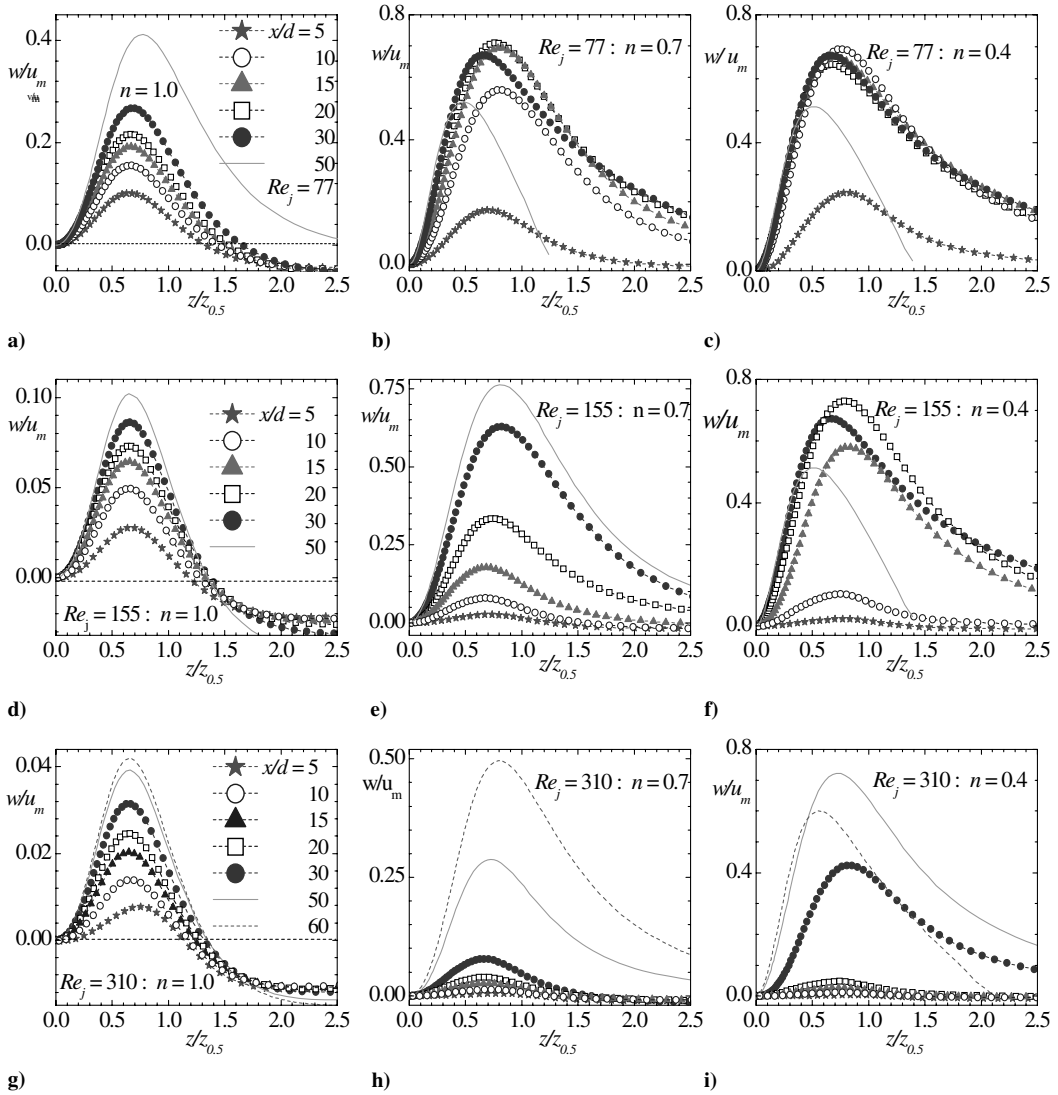

Fig. 10 The *w*-velocity profiles in transverse direction at various downstream locations for Newtonian a), d), and g) and non-Newtonian fluids $n = 0.7$ b), e), and h) and $n = 0.4$ c), f), and i).

fluid is a consequence of the rapid decay of u_m and the concomitant fast spread of the jet. At $x/d = 20$ and $Re_j = 77$, for example, $u_m/u_j = 5.88 \times 10^{-4}$ and $z_{0.5}/d = 20$ (20% of the entire channel height). It was shown in Fig. 3a that the profiles of u/u_m vs z/d from a smaller flow domain (height of $101d$) and a relatively larger flow domain (height of $151d$) for both $n = 1$ and $n = 0.4$ at $x/d = 20$ and $Re_j = 77$ were identical. Therefore, the lack of collapse observed in Fig. 7 cannot be attributed to confinement effects. In their boundary layer analysis [24–26], it was suggested that the shear stress terms in the viscosity equation might remove the possibility of a similarity solution. Furthermore, Schowalter [27] suggested that the possibility of the similarity for the 3-D boundary layer depends on the nature of definition describing the effective viscosity.

A comparison of representative velocity profiles for the fluids at a fixed streamwise location ($x/d = 20$) for all Re_j values is presented in Fig. 8. To better reveal differences among the profiles close to the wall, the profiles in the transverse direction (Figs. 8a, 8c, and 8e) are terminated at $z/z_{0.5} = 1.0$. In the transverse direction, the viscous nonlinearity effect is observed in the profiles of the non-Newtonian fluids ($n = 0.7$, 0.4) where they increase more rapidly from the no-slip boundary condition to the location of the maximum velocity. Because the inner region is akin to a boundary layer flow, one would expect the flow close to the wall to be primarily dominated by viscous effects. Similar to the results presented by Filip et al. [6], in the inner region, the shear-thinning fluids ($n = 0.4$ and 0.7) have higher normalized velocities than the Newtonian fluid. The discrepancy among the profiles in the near-wall region is more pronounced for the lowest Reynolds number ($Re_j = 77$). At this Re_j, the location of u_m (i.e., $z_m/z_{0.5}$) moves closer to the wall as n decreases. As a result, the inner layer becomes thinner as the fluid becomes more shear thinning. In the spanwise directions, the profiles at the lower Reynolds numbers ($Re_j = 77$ and 155) are nearly independent of n. At $Re_j = 310$, however, the fluid with $n = 0.4$ deviates from those with higher n.

The spanwise velocity profiles (v/u_m) along a line parallel to the wall passing through z_m are shown in Fig. 9. It is observed that the flow never reached a self-similar state. Notwithstanding the above comment, most of the profiles for the Newtonian fluid ($n = 1$) at $Re_j = 155$ and 310 do not deviate substantially from one another. It is noteworthy that v_m for all three Reynolds numbers occur at the same location of $y/y_{0.5} = 0.8$. At the higher Reynolds numbers, the values of v/u_m for the non-Newtonian fluids are generally an order of

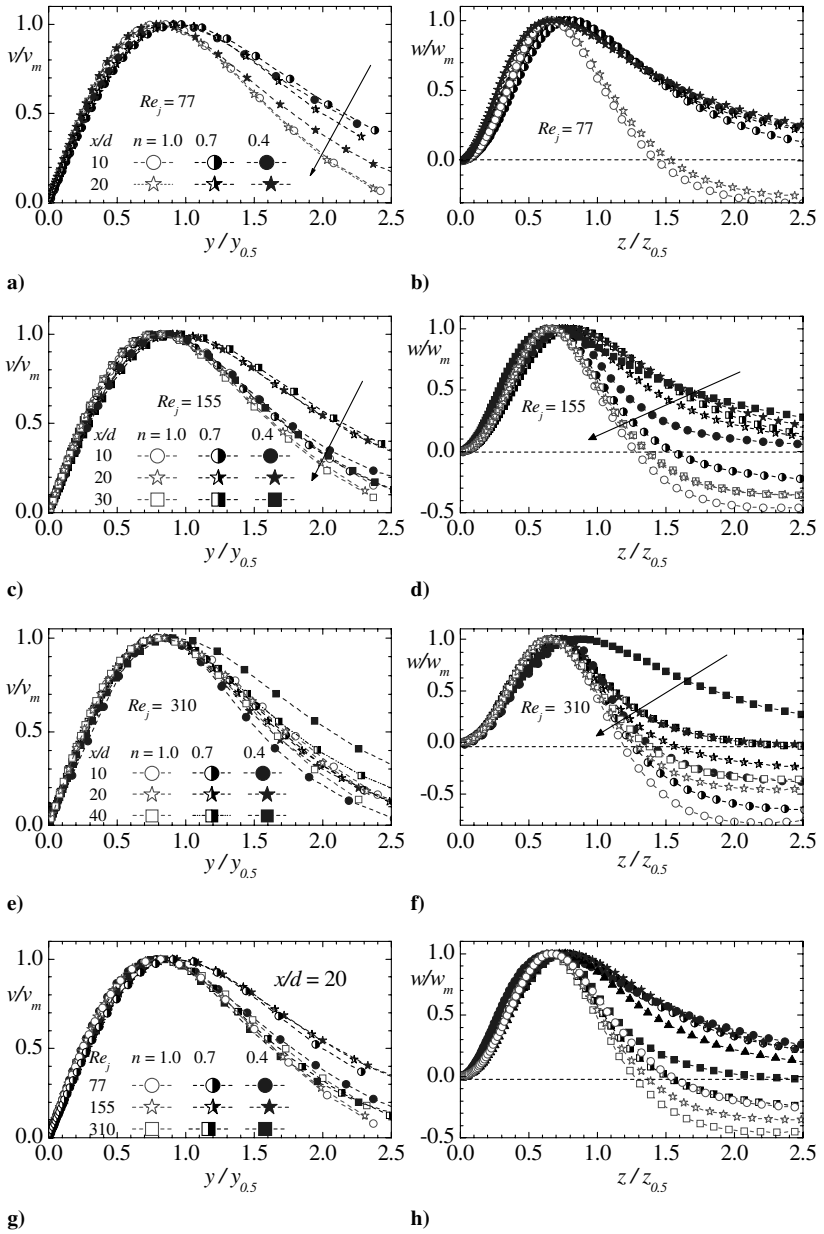

Fig. 11 Localized normalization of *v* and *w* velocities a)–f) and their variation with Re_j g), h) at $x/d = 20$.

magnitude higher than the corresponding data for the Newtonian fluid.

The transverse velocity profiles (w/u_m) at the symmetry plane are shown in Fig. 10. The profiles for $n = 1$ increase from zero to the maximum value and decrease in the outer region. This trend is observed at all the locations presented irrespective of the Reynolds number. The peak values (w/u_m) occur at the same location, $z/z_{0.5} = 0.65$, which is farther away from the wall than the location at which u_m occurred ($z/z_{0.5} \approx 0.5$). This location is also independent of Reynolds number. The outer region ($z/z_{0.5} > 1.5$) shows that there is an insignificant difference among the profiles at the compared downstream locations irrespective of the Reynolds number. The trends for $n = 0.4$ and 0.7 are similar to those observed for $n = 1.0$. Similarly, values of w are significantly higher than those for $n = 1.0$ but in these cases, w_m occurred at $z/z_{0.5} \approx 0.75$–0.82. Figures 9 and 10 demonstrate that the secondary velocities are substantially higher for the non-Newtonian fluids ($n = 0.7$ and 0.4) compared with those for the Newtonian fluid.

Figures 11a–11f show the profiles of v and w normalized by their respective local maximum values (v_m and w_m). Irrespective of the fluid type, the profiles in the inner region ($y/y_{0.5} < 1.2$ and $z/z_{0.5} < 1.0$) collapsed significantly better, especially those at higher Reynolds numbers. Significant differences are found, however, among the profiles in the outer region. These differences appear to be larger for the non-Newtonian fluids and depend strongly on the nature of fluid, that is, as the fluid become more shear thinning, the larger the disparity among the profiles. It is also important to note that at a higher Re_j, secondary flows are relatively insensitive to the fluid behavior. Notwithstanding the significant difference observed in Figs. 9 and 10 among various Reynolds numbers for all the fluids, the velocity scale used in Fig. 11 significantly improved collapse among the various profiles, especially in the inner region. In Figs. 11g and 11h, profiles at various Reynolds numbers at a fixed $x/d = 20$ are compared. In both plots, excellent agreement is observed in the regions $y/y_{0.5} < 1$ and $z/z_{0.5} < 1$.

Figures 12a–12d show the decay of v_m and w_m in the streamwise direction. In Figs. 12a and 12b, v_m and w_m are normalized by u_j, whereas in Figs. 12c and 12d, they are normalized by the local maximum streamwise velocity u_m. Irrespective of the fluid and Re_j, both v_m and w_m decayed with x/d, and in all cases their values are only a small fraction of u_j. On the other hand, values of v_m/u_m and w_m/u_m for the Newtonian fluid increase consistently with x/d. The trend for the $n = 0.7$ fluid at $Re_j = 310$ is similar to those for $n = 1$. However, v_m/u_m and w_m/u_m values for the non-Newtonian fluid ($n = 0.7$) are significantly higher (up to 3 times) compared with values for $n = 1$ at the same Re_j of 310. The $n = 0.4$ fluid at all Re_j and $n = 0.7$ fluid at $Re_j = 77$ and 155 show an interesting trend. These profiles increase at the early stages of flow development to a peak value and then decrease.

IV. Conclusions

Three-dimensional laminar wall-jet flows of both Newtonian fluid ($n = 1.0$) and two shear-thinning non-Newtonian fluids ($n = 0.4$ and 0.7) were numerically investigated. For each fluid, the wall-jet characteristics including the decay of the maximum streamwise velocity (u_m), jet half-width in both transverse and spanwise directions ($z_{0.5}$ and $y_{0.5}$), and similarity velocity profiles were studied in detail for three initial jet Reynolds numbers ($Re_j = 77$, 155, and 310). The results clearly demonstrate that the velocity decay, spread of the jet, and skin friction coefficient depend strongly on both Re_j and the specific fluid. For a given fluid, the velocity decay is more rapid at a lower Re_j because the initial jet momentum is expended more quickly. When Re_j is kept constant, it was obvious that the variation of u_m with x/d could be divided into an initial region and a final region. In the latter, the velocity decay is more rapid for the shear-thinning non-Newtonian fluids than the Newtonian fluid, whereas the reverse is true in the initial region. The demarcations between the initial and final regions were $x/d = 5$, 10, and 22, respectively, for $Re_j = 77$, 155, and 310. Even for the two

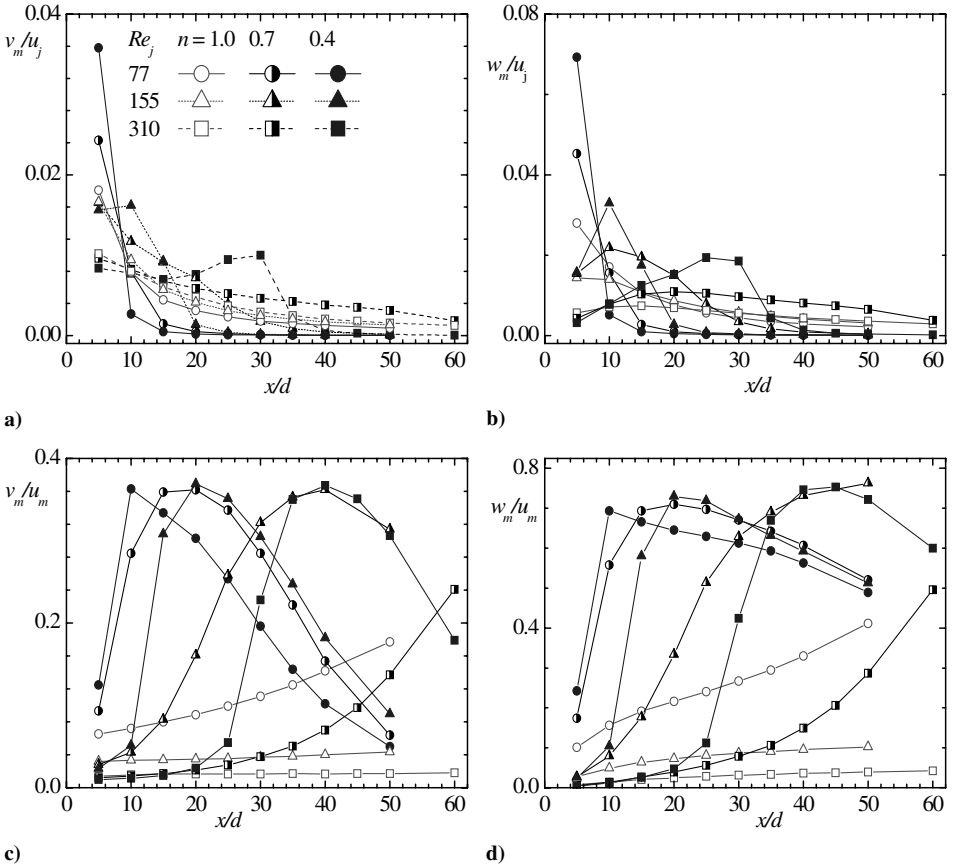

Fig. 12 Streamwise variation of normalized v_m and w_m: v_m/u_j a), w_m/u_j b), v_m/u_m c), and w_m/u_m d).

non-Newtonian fluids, the decay of u_m is faster for the more shear-thinning fluid ($n = 0.4$) than the fluid with $n = 0.7$. This observation was attributed to the notion that the apparent viscosity at any downstream location increased dramatically when the fluid becomes more shear thinning. Therefore, for fluid with similar Re_j, the local Reynolds number for the non-Newtonian shear-thinning fluids becomes substantially smaller than for the Newtonian fluid. The decay of u_m with x/d is accompanied by an increase in z_m, $z_{0.5}$, and $y_{0.5}$. As expected, these values are higher at a lower Re_j (for a given fluid) and for a more shear-thinning fluid (at a given Re_j). Furthermore, the jet spreads much faster in the transverse direction than in the spanwise direction irrespective of Re_j and the fluid; however, $y_{0.5}/z_{0.5} = 0.5 \pm 0.15$ for all the fluids and Reynolds number investigated.

For the Newtonian fluid, the streamwise velocity profiles in both transverse and spanwise directions became self-similar at $x/d \geq 5$ irrespective of Re_j. For the non-Newtonian fluid with $n = 0.7$, self-similarity conditions were observed only at $Re_j = 155$ and 310. The results demonstrate a genuine lack of self-similarity for the more shear-thinning fluid ($n = 0.4$). Because the inner layer is akin to a classical boundary layer, significant differences were observed among the velocity profiles for various fluids at a fixed Re_j. In this region, the normalized velocities at identical normalized distance from the wall are larger as the fluid becomes more shear thinning. The spanwise and transverse components of the velocities for the non-Newtonian fluids are generally an order of magnitude larger than the corresponding values for the Newtonian fluid. Irrespective of the specific fluid or Reynolds number, the profiles of the spanwise and transverse velocities show self-similar behavior in the inner region when they are normalized by their respective local peak values.

Acknowledgments

M. F. Tachie gratefully acknowledges the financial support provided by Natural Sciences and Engineering Research Council of Canada (Discovery Grant).

References

[1] Launder, B. E., and Rodi, W., "The Turbulent Wall Jet," *Progress in Aerospace Sciences*, Vol. 19, No. 1, 1979, pp. 81–128. doi:10.1016/0376-0421(79)90002-2

[2] Glauert, M. B., "The Wall Jet," *Journal of Fluid Mechanics*, Vol. 1, No. 6, 1956, pp. 625–643. doi:10.1017/S002211205600041X

[3] Bajura, R. A., and Szewczyk, A. A., "Experimental Investigation of a Laminar Two-Dimensional Plane Wall Jet," *Physics of Fluids*, Vol. 13, No. 7, 1970, pp. 1653–1664. doi:10.1063/1.1693137

[4] Cohen, J., Amitay, M., and Bayly, B. J., "Laminar-Turbulent Transition of Wall-Jet Flows Subjected to Blowing and Suction," *Physics of Fluids A*, Vol. 4, No. 2, 1992, pp. 283–289. doi:10.1063/1.858304

[5] Gorla, R. S. R., and Jeng, D. R., "Laminar Plane Wall Jet," *Proceedings of the 12th Midwestern Mechanics Conference: Developments in Mechanics*, University of Notre Dame, West Bend, IN, Vol. 6, No. 8, 1971, pp. 137–151.

[6] Filip, P., Kolar, V., and Hajek, R., "Similarity Prediction of Wall Jets Past Axisymmetric Bodies for Power-Law Fluids," *Acta Mechanica*, Vol. 88, Nos. 3–4, 1991, pp. 167–173. doi:10.1007/BF01177094

[7] Gorla, R. S. R., "Laminar Wall Jet of a Non-Newtonian Fluid over a Curved Surface," *Journal of Applied Mechanics*, Vol. 51, No. 2, 1984, pp. 440–443.

[8] Craft, T. J., and Launder, B. E., "On the Spreading Mechanism of the Three-Dimensional Turbulent Wall Jet," *Journal of Fluid Mechanics*, Vol. 435, No. 1, 2001, pp. 305–326. doi:10.1017/S0022112001003846

[9] Krechetnikov, R., and Lipatov, I., "Hidden Invariances in Problems of Two-Dimensional and Three-Dimensional Wall Jets For Newtonian and Non-Newtonian Fluids," *Journal of Applied Mathematics*, Vol. 62, No. 6, 2002, pp. 1837–1855.

[10] Tetervin, N., "Laminar Flow of a Slightly Viscous Incompressible Fluid That Issues from a Slit and Passes over a Flat Plate," NACA TN 1644, 1948.

[11] Gorla, R. S. R., "Unsteady Heat Transfer Characteristics of a Two Dimensional Laminar Wall Jet," *International Journal of Engineering Science*, Vol. 11, No. 8, 1973, pp. 841–850. doi:10.1016/0020-7225(73)90033-5

[12] Issa, J. S., "Numerical Computation of the Heat Transfer and Fluid Mechanics in the Laminar Wall Jet and Comparison to the Self-Similar Solutions," *ASME International Mechanical Engineering Congress and Exposition*, IMECE04, American Society of Mechanical Engineers, Fairfield, NJ, Vol. 375, No. 3, 13–20 Nov. 2004, pp. 191–197.

[13] Issa, J. S., "Scaling of Convective Heat Transfer in Laminar and Turbulent Wall Jets with Effects of Freestream Flow and Forcing," Ph.D. Dissertation, Aerospace and Mechanical Engineering Department, The University of Arizona, Tucson, AZ, 2006.

[14] Bird, R. B., Armstrong, R. C., and Hassager, O., *Dynamics of Polymeric Liquids in Fluid Mechanics*, 2nd ed., Wiley, New York, Vol. 1, 1987.

[15] Ferziger, J. H., and Perić, M., *Computational Methods for Fluid Dynamics*, 3rd ed., Springer-Verlag, Berlin, 1995, Chaps. 3–8.

[16] Wu, J., and Thompson, M. C., "Non-Newtonian Shear-Thinning Flows Past a Flat Plate," *Journal of Non-Newtonian Fluid Mechanics*, Vol. 66, Nos. 2–3, 1996, pp. 127–144. doi:10.1016/S0377-0257(96)01476-0

[17] Dressler, D. M., "An Experimental Investigation of Newtonian and Non-Newtonian Spray Interaction with a Moving Surface," M.Sc. Thesis, Mechanical Engineering Department, The Faculty of Graduate Studies, The University of British Columbia, Vancouver, BC, Canada, 2006.

[18] Khosla, P. K., and Rubin, S. G., "A Diagonally Dominant Second-Order Accurate Implicit Scheme," *Computers and Fluids*, Vol. 2, No. 2, 1974, pp. 207–209. doi:10.1016/0045-7930(74)90014-0

[19] Patankar, S. V. M., *Numerical Heat Transfer and Fluid Flow*, Taylor and Francis, London, 1980.

[20] Rhie, C. M., and Chow, W. L., "Numerical Study of the Turbulent Flow Part an Airfoil with Trailing Edge Separation," *AIAA Journal*, Vol. 21, No. 11, 1983, pp. 1525–1532. doi:10.2514/3.8284

[21] Van Doormaal, J. P., and Raithby, G. D., "Enhancements of the SIMPLE Method for Predicting Incompressible Fluid Flows," *Numerical Heat Transfer*, Vol. 7, No. 2, 1984, pp. 147–163. doi:10.1080/01495728408961817

[22] Stone, H. L., "Iterative Solution of Implicit Approximations of Multi-Dimensional Partial Differential Equations," *SIAM Journal on Numerical Analysis*, Vol. 5, No. 3, 1968, pp. 530–558. doi:10.1137/0705044

[23] Lilek, Z., Muzaferija, S., and Perić, M., "Efficiency and Accuracy Aspects of a Full-Multigrid Simple Algorithm for Three-Dimensional Flows," *Numerical Heat Transfer, Part B, Fundamentals*, Vol. 31, No. 1, 1997, pp. 23–42. doi:10.1080/10407799708915097

[24] Gutfinger, C., and Shinnar, R., "Velocity Distributions in Two-Dimensional Laminar Liquid-to-Liquid Jets in Power-Law Fluids," *AIChE Journal*, Vol. 10, No. 5, 1964, pp. 631–639. doi:10.1002/aic.690100512

[25] Denier, J. P., and Hewitt, R. E., "Asymptotic Matching Constraints for a Boundary-Layer Flow of a Power-Law Fluid," *Journal of Fluid Mechanics*, Vol. 518, 2004, pp. 261–279. doi:10.1017/S0022112004001090

[26] Acrivos, A., Shah, M. J., and Petersen, E. E., "Momentum and Heat Transfer in Laminar Boundary-Layer Flows of Non-Newtonian Fluids Past External Surfaces," *AIChE Journal*, Vol. 6, No. 2, 1960, pp. 312–317. doi:10.1002/aic.690060227

[27] Schowalter, W. R., "The Application of Boundary-Layer Theory to Power-Law Pseudoplastic Fluids: Similar Solutions," *AIChE Journal*, Vol. 6, No. 1, 1960, pp. 24–28. doi:10.1002/aic.690060105

C. Kaplan
Associate Editor